Device performance: To obtain low-driving-voltage optical modulators for band-operation, we designed them to have large induced phases $|\phi|$, by varying the lengths L_1 and L_2. We considered an electrode structure with the following parameters. The gap between the electrodes of ACPWs and CPWs is 27 µm. The width and the thickness of the electrodes are, respectively, 5 and 20 µm. The characteristic coefficients of the modulating electrode (ACPW) are $\gamma_1 = 14.5 + j598.1$ and $Z_{01} = 52.5\ \Omega$. Those for the stub (CPW) are $\gamma_2 = 16.0 + j550.0$ and $Z_{02} = 44.5\ \Omega$. Using (3), we obtained a combination of L_1 and L_2 that gave a maximum $|\phi|$. When $L_1 = 1.41\lambda_1 = 14.81$ mm and $L_2 = 0.12\lambda_2 = 1.37$ mm, $|\Phi|$ had a maximum of 1.38 at 10 GHz, where λ_1 and λ_2 were the wavelengths on the modulating electrode and the stub, respectively. $2L_p$ was set to be $3 \times (c/fn_0)$. As shown in Fig. 2, the normalised induced phase of the fabricated reflection-type modulator for the 1.55 µm region (solid line) was larger than that of the conventional structure where the optical reflection was not used (dashed line). The V_π was 2.9 V at 7 GHz and 3.4 V at 10.5 GHz, while that of the conventional structure was 5.8 V at 10.5 GHz.

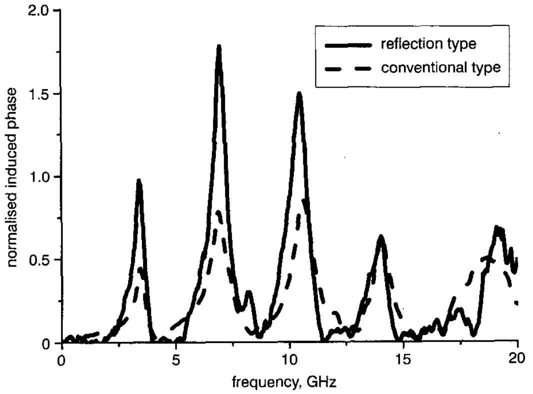

Fig. 2 *Normalised induced phase of fabricated modulator*

Conclusion: We have developed an LiNbO3 modulator with lightwave reflection and double-stub structure. The modulator has a reflection-type Mach-Zehnder interferometer consisting of a Y-branch and a pair of optical reflections. The halfwave voltage was 2.9 V at 7 GHz. The proposed structure provides very low driving voltage for band-operation, without using complicated three-dimensional waveguide structures.

19 July 2002
Electronics Letters Online No: 20020802
DOI: 10.1049/el:20020802

T. Kawanishi, Y. Matsuo and M. Izutsu (*Basic and Advanced Research Division, Communications Research Laboratory, 4-2-1 Nukui-Kitamachi, Koganei, Tokyo 184-8795, Japan*)

S. Oikawa and K. Higuma (*New Technology Research Laboratories, Sumitomo Osaka Cement, 585 Toyotomi, Funabashi, Chiba 274-8801, Japan*)

References

1 KONDO, J., KONDO, A., AOKI, K., TAKATSUJI, S., MITOMI, O., IMAEDA, M., KOZUKA, Y., and MINAKATA, M.: 'High-speed and low-driving-voltage X-cut LiNbO$_3$ optical modulator with two step backside slot', *Electron. Lett.*, 2002, **38**, pp. 472–473

2 HOWERTON, M.M., MOELLER, R.P., GREENBLATT, A.S., and KAÖHENBÜHL, R.: 'Fully packaged broad-band LiNbO$_3$ modulator with low drive voltage', *IEEE Photonics Technol. Lett.*, 2000, **12**, pp. 792–794

3 BURNS, W.K., HOWERTON, M.M., MOELLER, R.P., GREENBLATT, A.S., and MCELANON, R.W.: 'Broad-band reflection traveling-wave LiNbO$_3$ modulator', *IEEE Photonics Technol. Lett.*, 1998, **10**, pp. 805–806

4 KAWANISHI, T., OIKAWA, S., HIGUMA, K., SASAKI, M., and IZUTSU, M.: 'Design of LiNbO$_3$ optical modulator with an asymmetric resonant structure', *IEICE Trans. Electron.*, 2002, **E85-C**, pp. 150–155

5 KAWANISHI, T., OIKAWA, S., HIGUMA, K., MATSUO, Y., and IZUTSU, M.: 'LiNbO$_3$ resonant-type optical modulator with double-stub structure', *Electron. Lett.*, 2001, **37**, pp. 1244–1246

Optimum redundant array configurations for Earth observation aperture synthesis microwave radiometers

I. Corbella, A. Camps, N. Duffo and M. Vall-llossera

Two-dimensional aperture synthesis radiometry is the technology selected for ESA's SMOS mission to provide high resolution L-band radiometric imagery. The array topology is a Y-shaped structure. The position and number of redundant elements to minimise instrument degradation in case of element failure(s) are studied.

Introduction: The MIRAS instrument [1, 2], single payload of the European Space Agency's SMOS mission, will be the first two-dimensional aperture synthesis radiometer for Earth observation. It will operate at L-band, where there is a good sensitivity to the soil moisture content and the sea surface salinity, the atmosphere is almost transparent, and there is a frequency band reserved for passive observations. The imaging is performed through a Fourier synthesis process of the cross-correlations V_{12} measured between the bandpass signals $b_1(t)$ and $b_2(t)$, centered at f_0, $\lambda_0 = c/f_0$, collected by every pair of antennas. If all the antennas have the same antenna radiation pattern $|F_n(\xi, \eta)|^2$ and spatial decorrelation effects are negligible, the relationship between the brightness temperature and the observables is

$$\begin{aligned} V_{12} &= V(u_{12}, v_{12}) \overset{\Delta}{=} \frac{1}{\mathrm{k_B BG}} \cdot \frac{1}{2} \langle b_1(t)\, b_2^*(t) \rangle \\ &= \frac{1}{\Omega} \iint_{\xi^2+\eta^2 \le 1} \frac{T_B(\xi, \eta) |F_n(\xi, \eta)|^2}{\sqrt{1 - \xi^2 - \eta^2}} \\ &\quad \times \exp(-j2\pi(u_{12}\xi + v_{12}\eta))\, d\xi d\eta \end{aligned} \tag{1}$$

where $\mathrm{k_B}$ is the Boltzmann's constant, B and G are the receivers' noise bandwidth and power gain, Ω is the solid angle of the antennas, the spatial frequency sampled (baseline) depends on the antenna position difference: $(u_{12}, v_{12}) = (x_2 - x_1, y_2 - y_1)/\lambda_0$, and the director cosines $(\xi, \eta) = (\sin\theta\cos\phi, \sin\theta\sin\phi)$ are defined with respect to the X and Y axes.

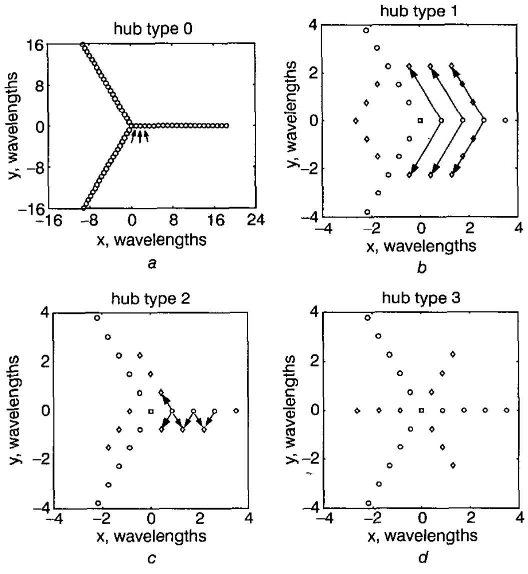

Fig. 1 *Hub configurations*

a Array configuration without redundancy: each circle represents an antenna position (NEL = 21 antennas per arm spaced $d = 0.875$ wavelengths, SMOS/MIRAS configuration), the square represents a noise injection radiometer used to measure $V(0, 0)$, its output is not correlated with rest of the antennas
b Hexagonal hub
c Helix hub
d Star hub
Redundant antennas marked with diamonds, arrows indicate redundant baselines

Since $\xi^2+\eta^2 \leq 1$, $V(u, v)$ is optimally sampled over a (u, v) hexagonal grid, as provided by a Y-array, which additionally provides the largest (u, v) coverage, and therefore achieves the best angular resolution [3]. The loss of (u, v) points due to element failure(s) distorts the instrument's spatial response named equivalent array factor (AF_{eq}) [4], and degrades the radiometric sensitivity and accuracy [5]. In [5] it is shown that the failure of a single element degrades the spatial resolution by less than 10%, but the radiometric accuracy degrades very quickly: from ~4.5 to ~13 K for the single failure of one element in positions 8 to 1 (Fig. 1*a* in [5]). The most critical elements are those closest to the array centre, since they lead to the shortest baselines, for which $V(u, v)$ has the largest amplitude. Owing to the stringent performances required to monitor the soil moisture and the ocean salinity it is clear that the loss of an element will lead to unacceptable degradation of the instrument performances. Therefore, it is necessary to analyse the use of redundant elements to minimise system performance degradation in case of failure.

Hub configurations with redundant elements: Owing to physical size, mass and power consumption limitations, the number of redundant elements must be limited. During SMOS phase A it was decided to add redundancy only to the first three elements of each arm. The three hubs under study are shown in Figs. 1*a–d*. Hub 0 (Fig. 1*a*) has no redundant elements and it is the original array configuration. Hub 1 forms an hexagon of 15 redundant elements around the central one (Fig. 1*b*). Hub 2 adds nine redundant elements parallel to the Y-arms (Fig. 1*c*). And hub 3 adds nine redundant elements in the homothetic positions of the first elements of each arm (Fig. 1*d*). From the three hubs, only hubs 1 and 3 provide two replacements for every main element in the hub (marked as arrows in Figs. 1*b–d*). Hub 3 has less redundant elements than hub 1, because each spare antenna can replace two main antennas. However, hub 2 can be extended to have spare elements at both sides of each arm, at the expense of an excessive increase in the number of redundant elements (15 in total).

Table 1: Equivalent array factor parameters for different array/hub configurations in case of failure

Hub configuration	Parameter	No failure	Failure of antennas 1, 2 and 3 of an arm
Fig. 1*a*	SLL	14.5 db	11.3 dB
	$MBE_{10\ dB}$	96.8%	99.3%
	MBE_{SSL}	100.4%	103.7%
	(u, v) points	2767	2509
Fig. 1*b*	SLL	14.8 dB	14.8 dB
	$MBE_{10\ dB}$	96.6%	96.6%
	MBE_{SSL}	100.1%	100.2%
	(u, v) points	2827	2823
Fig. 1*c*	SLL	14.3 dB	12.7 dB
	$MBE_{10\ dB}$	97.0%	95.1%
	MBE_{SSL}	100.6%	98.3%
	(u, v) points	2791	2749
Fig. 1*d*	SLL	14.3 dB	14.0 dB
	$MBE_{10\ dB}$	96.9%	97.0%
	MBE_{SSL}	100.5%	100.7%
	(u, v) points	2791	2767

Redundant antennas recover most of instrument capabilities

SLL: side lobe level; MBE_z: main beam efficiency at 'z' level below maximum

System performance in case of element failure: The three hub configurations provide full replacement of a single element failure. The worst case then happens when the first three elements of one arm fail simultaneously. Table 1 summarises the performance in this situation, indicating the number of (u, v) points before and after the failure, the side lobe level (SLL) of the AF_{eq} and the main beam efficiency or MBE (ratio of energy collected through the main beam compared to the total energy) at −10 dB and at the SLL [4]. Figs. 2*a* and *b* show the (u, v) coverage after the failure of the first three elements of an arm for hubs 0 and 3, and Figs. 2*c* and *d* show the corresponding AF_{eq}.

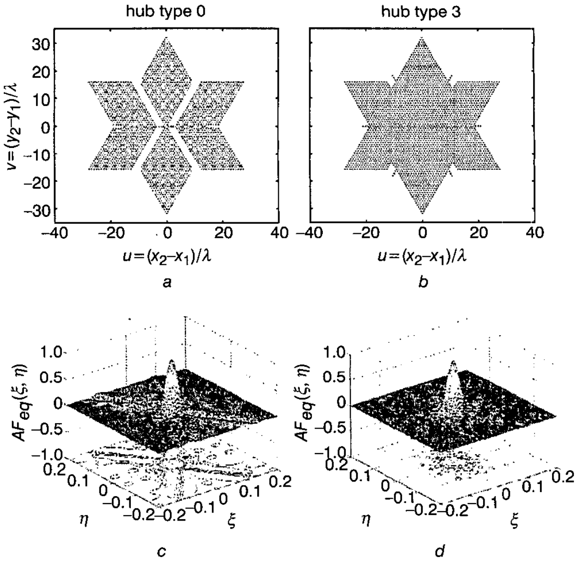

Fig. 2 *Associated (u, v) spatial frequency coverage in case of failure of elements 1, 2, 3 when all redundant elements are ON, and equivalent array factor (system impulse response) corresponding to hubs 0 and 3*

a and *c* Hub 0, no redundancy
b and *d* Hub 3

Hub 1 provides the best recovery of missing (u, v) points, but hub 3 is the most effective one in terms of array performance degradation after element failure(s) (see performance comparison between hub 3 in case of failure and hub 0 in case of no failure or hub 1 in case of failure). Hub 2 has limited capabilities for element failure replacement, since it cannot fully replace failure of the third element (two complete lines of (u, v) points are missing, instead of 12 in Fig. 2*a*), unless a second set of spare elements is added to each arm, which increases the number of elements to 15.

Since the T_B image is formed through a Fourier synthesis process, the AF_{eq} has negative sidelobes, and the MBE can be higher than 100%. In case of element failure(s) the AF_{eq} is very similar for hubs 1 and 3, and the MBE remains almost unchanged. Fig. 2*c* shows the AF_{eq} for hub 0. In this case, the amplitude of the negative side lobes increases significantly reducing the total energy collected, and increasing the MBE. In all cases, the SLL slightly worsens.

Conclusions: Hub 1 is slightly better than hub 3 in terms of SLL, but hub 3 is slightly better than hub 1 in terms of MBE. In terms of mass and power consumption hub 1 has 15 spare elements, hub 2 has nine elements (although its performances can be improved adding $3 \times 5 = 15$ elements between the Y-arms), and hub 3 has nine elements. Therefore, hub 3 was the recommended option, which is the one currently being implemented in the SMOS project. Size, mass and power consumption permitting, further redundant elements could be added at the homothetic positions of elements 4, 5, etc., of each arm following the star hub configuration.

Acknowledgments: This work has been supported by the Spanish Comisión Interministerial de Ciencia y Tecnología (grant CICYT TIC 99-1050-C03-01), and by EADS-CASA Space Division (Madrid, Spain), prime contractor of SMOS Extended Phase A Activities.

3 May 2002
Electronics Letters Online No: 20020816
DOI: 10.1049/el:20020816

I. Corbella, A. Camps, N. Duffo and M. Vall-llossera (*Department of Signal Theory and Communications, Polytechnic University of Catalonia, Campus Nord, D3 E-08034 Barcelona, Spain*)

E-mail: corbella@tsc.upc.es

References

1 MARTÍN-NEIRA, M., and GOUTOULE, J.M.: 'MIRAS – a two-dimensional aperture-synthesis radiometer for soil-moisture and ocean salinity observations', *ESA Bull.*, 1997, (92), pp. 95–104

2 SIVESTRIN, P., BERGER, M., KERR, Y., and FONT, J.: 'ESA's Second Earth Explorer Opportunity Mission: The Soil Moisture and Ocean Salinity Mission – SMOS', *IEEE Geosci. Remote Sens. Newsl.*, 2001, (118), pp. 11–14

3 CAMPS, A., BARÁ, J., CORBELLA, I., and TORRES, F.: 'The processing of hexagonally sampled signals with standard rectangular techniques: application to 2D large aperture synthesis interferometric radiometers', *IEEE Trans. Geosci. Remote Sens.* GRS-35, 1997, pp. 183–190

4 BARÁ, J., CAMPS, A., TORRES, F., and CORBELLA, I.: 'Angular resolution of two-dimensional hexagonally sampled interferometric radiometer', *Radio Sci.*, 1998, **33**, (5), pp. 1459–1473

5 VALL-LLOSSERA, M., DUFFO, N., CAMPS, A., CORBELLA, I., TORRES, F., and BARÁ, J.: 'Reliability analysis in aperture synthesis interferometric radiometers: application to L-band MIRAS instrument', *Radio Sci.*, 2001, **36**, (1), pp. 107–117

SAR interferometric phase statistics in wavelet domain

C. López and X. Fàbregas

Synthetic aperture radar (SAR) interferometry is employed to obtain topographic information. Owing to noise, interferometric information has to be filtered. The wavelet transform can be employed to filter the interferometric phase, maintaining the spatial resolution, but new signal models have to be studied in this domain for further processing.

Introduction: Synthetic aperture radar interferometry (InSAR) is an established technique to obtain information about the earth's surface topography. The interferometric phase is calculated as the phase difference between two complex SAR images from the same area, but taken from slightly different positions. Owing to the lack of interferometric coherence $|\gamma|$ between both SAR images, the interferometric phase is noisy. In addition, the interferometric phase is only known within the interval $[-\pi, \pi)$, it being necessary to unwrap it to recover unambiguously the height information. The unwrapping process is also affected by phase noise, since it induces phase residues. Phase filtering is thus necessary to reduce noise effects.

In the last decade, the wavelet transform (WT) has shown a big potential for image processing applications. In the field of SAR data processing, the use of the WT is emerging since it allows processing of SAR imagery, keeping the spatial resolution and image details.

Since the physics behind SAR data is completely different from that of optical images, any data processing has to take this into account. Thus, it is necessary to review or even to define new noise models adapted to this problem. In this Letter, we provide a study of a signal model for the interferometric phase in the wavelet domain. This model is validated with real interferometric data.

Complex interferometric phase noise model: Earth topography can be represented locally by a constant slope [1], thus the interferometric phase ϕ_x can be assumed to be a constant phase ramp. In the spatial domain the measured interferometric phase complies with the model $\phi_z = \phi_x + v$ [2], where v is a phase noise term. The real and imaginary parts of the measured phase ϕ_z coded in the unit circle, defined as the complex interferometric phase, can be modelled by [3, 4]:

$$\cos(\phi_z) = N_c \cos(\phi_x) + v_c \tag{1}$$

$$\sin(\phi_z) = N_c \sin(\phi_x) + v_s \tag{2}$$

the wavelet transforms of which are [3]:

$$\mu_1 = DWT_{2D}\{\cos(\phi_z)\} = 2^i N_c \cos(\phi_x^w) + v_c^w \tag{3}$$

$$\mu_2 = DWT_{2D}\{\sin(\phi_z)\} = 2^i N_c \sin(\phi_x^w) + v_s^w \tag{4}$$

where i represents the wavelet scale. v_c^w and v_s^w are noise terms independent from the wavelet scale. The phase term ϕ_x^w represents the interferometric phase in the wavelet domain, which contains the same information as ϕ_x. The WT is able to localise ϕ_x in the space-frequency plane. N_c has a one-to-one relation with the coherence $|\gamma|$ providing, thus, the same information [3, 4].

For a constant interferometric phase and homogeneous noise (i.e. constant $|\gamma|$), the parameter N_c, as well as the terms $\cos(\phi_x^w)$ and $\sin(\phi_x^w)$ are constant. Therefore, signal randomness is only due to v_c^w and v_s^w. The discrete wavelet transform (DWT) can be seen as the addition of (weighted) random variables. By the central limit theorem, the weighted sum of identically distributed random variables can be approximated by a Gaussian distribution. Therefore, v_c^w and v_s^w are approximately Gaussian distributed. To test it, avoiding any interference from the phase ϕ_x^w, a constant slope producing 20 pixel fringes, corrupted with a noise equivalent to a coherence $|\gamma| = 0.6$, has been simulated. Table 1 shows a statistical test applied over the real part of the interferometric complex phase in the wavelet domain. As shown, since the useful signal is concentrated in the low frequency band (LL), the wavelet bands (HL, LH and HH) present a kurtosis close to 3 and the significance levels for the Kolmogorov-Smirnov (KS) test, assuming a Gaussian distribution, are high. These results demonstrate that v_c^w and v_s^w can be described by a Gaussian distribution. The same agreement is observed for any other value of $|\gamma|$, and for the imaginary part of the complex interferometric phase in the wavelet domain. The LL band deserves special attention. In this case, as there is signal content, the signal model will be represented by the real and imaginary parts of $\exp(j\phi_x^w)$ plus a Gaussian noise. Therefore, in this case, the amplitude $|\mu_1 + j\mu_2|$ has a Rice distribution. This result is equally valid for the rest of the wavelet bands. The amplitude in the wavelet domain will be Rayleigh distributed for $|\gamma| = 0$, in a particular space-frequency region, and Rice distributed for $|\gamma| > 0$

Table 1: Kurtosis and KS significance levels (Gaussian assumption) for real part of simulated complex interferometric phase ramp in wavelet domain

	Horizontal band (HL)		Vertical band (LH)		Diagonal band (LL)	
	Kurtosis	KS significance level (%)	Kurtosis	KS significance level (%)	Kurtosis	KS significance level (%)
Scale 1	2.98	87.93	2.98	79.83	2.94	98.34
Scale 2	3.03	95.78	2.97	86.08	3.00	66.15
Scale 3	3.08	82.87	2.95	85.32	3.00	82.87

Complex interferometric phase signal model: The topographic model assumed previously (i.e. constant slope) does not take into account spatial details, which are important, for instance, in urban areas. Since no information is available about the distribution of the 'true' topographic phase ϕ_x, an *a priori* model for the spatial details is not available in the spatial domain. This drawback can be overcome in the wavelet domain. As mentioned in the preceding Section, the DWT can be interpreted as a weighted sum of random variables. Therefore, $DWT_{2D}\{N_c \cos(\phi_x)\}$ and $DWT_{2D}\{N_c \sin(\phi_x)\}$ can be supposed to be determined, as a first approximation, by a Gaussian distribution. Tests with real data (see Tables 2 and 3) show that wavelet statistics have kurtosis higher than 3. To take into account this deviation from Gaussian behaviour, a double stochastic model is proposed for the wavelet coefficients x:

$$p_x(x) = \int_0^\infty p_x(x\,|_{\sigma^2}) p_{\sigma^2}(\sigma^2) d\sigma^2 \tag{5}$$

where $p_x(x|_{\sigma^2})$ represents the Gaussian distribution of the wavelet coefficients and $p_{\sigma^2}(\sigma^2)$ is a generalised gamma distribution (GGD) modelling the variability of the variance through the phase image. $p_x(x)$ cannot be obtained in a general form. Numerical integration of (5), see Fig. 1, indicates that $p_x(x)$ can be assumed to be a GGD model. To test the validity of this model, two real interferometric phase images taken with the German sensor E-SAR from DLR have been employed. The first image is an X-band interferogram of Mount Etna (Italy) and the second one is an L-band interferogram of the Oberpfaffenhoffen test site (Germany), were man-made structures are present. These two interferometric phases were filtered with the algorithm presented in [3], which is based on maintaining the spatial resolution. Tables 2 and 3 present the kurtosis and the KS test significance levels, assuming a GGD model, applied to the real part of the filtered complex interfero-